FULL ARTICLE

Second harmonic generation microscopy as a powerful diagnostic imaging modality for human ovarian cancer

*Javier Adur**,1,2, *Vitor B. Pelegati*1, *Andre A. de Thomaz*1, *Mariana O. Baratti*3, *Liliana A. L. A. Andrade*4, *Hernandes F. Carvalho*3,5, *Fátima Bottcher-Luiz*3,6, *and Carlos Lenz Cesar*1,3

1 Biomedical Lasers Application Laboratory, Optics and Photonics Research Center, "Gleb Wataghin" Institute of Physics, State University of Campinas (UNICAMP), Brazil
2 Microscopy Laboratory Applied to Molecular and Cellular Studies, School of Bioengineering, National University of Entre Ríos (UNER), Ruta 11 Km10, Oro Verde 3101, Entre Ríos, Argentina
3 INFABiC, National Institute of Science and Technology on Photonics Applied to Cell Biology, Campinas, Brazil
4 Department of Pathology of the Faculty of Medical Sciences, State University of Campinas (UNICAMP), Brazil
5 Department of Anatomy, Cell Biology, Physiology and Biophysics, Biology Institute, State University of Campinas (UNICAMP), Brazil
6 Department of Obstetrics and Gynecology of the Faculty of Medical Sciences, State University of Campinas (UNICAMP), Brazil

In this study we showed that second-harmonic generation (SHG) microscopy combined with precise methods for images evaluation can be used to detect structural changes in the human ovarian stroma. Using a set of scoring methods (alignment of collagen fibers, anisotropy, and correlation), we found significant differences in the distribution and organization of collagen fibers in the stroma component of serous, mucinous, endometrioid and mixed ovarian tumors as compared with normal ovary tissue. This methodology was capable to differentiate between cancerous and healthy tissue, with clear cut distinction between normal, benign, borderline, and malignant tumors of serous type. Our results indicated that the combination of different image-analysis approaches presented here represent a powerful tool to

PICROSIRUS   TPEF + SHG   SHG
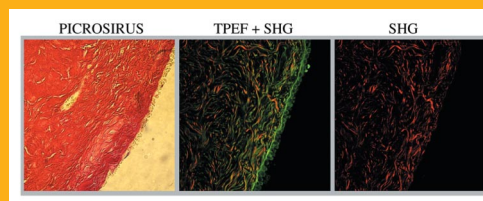
Slice of a sample of normal ovary labeled with picrosirius and two photon emission fluorescence and second harmonic generation microscopy images of H&E-stain adjacent section.

investigate collagen organization and extracellular matrix remodeling in ovarian tumors.

1. Introduction

Two-photon excited fluorescence (TPEF) and second harmonic generation (SHG) microscopy provide powerful tools to image cellular autofluorescence and extracellular matrix structure [1, 2]. Specifically, TPEF results from the nonlinear excitation of molecular fluorescence [3], while SHG signals depend on non-linear interactions of illumination with a non-centrosymmetric environment that can provide sub-micron resolution [2, 4].

SHG is a coherent process in both time and space, which means that it is instantaneous and the emission is anisotropic. In bulk materials SHG in a

* Corresponding author: e-mail: jadur@bioingenieria.edu.ar, Phone: 0054-343-4975100

crystal of a directional beam is emitted in one direction and only if the phase-matching condition (matching of light momentum) is fulfilled for a given polarization. There are two reasons why the phase-matching condition is relaxed in SHG microscopy. First the high numerical aperture incident beam is spreaded over a large angle range which enhances the chance that parts of the beam meet the phase-matching condition. Second because the phase-matching condition depends on the sample size with respect to the wavelength which is relaxed for small samples. This is the usual case in microscopy. Nonetheless, the phase matching condition still imposes restrictions on the emitted light directionality depending on the concentration, spacing, order or disorder and orientation of the 'scatterers' in the focal volume [5, 6]. Therefore, ordered non-centrosymmetric structures such as collagen fibrils generate a strong SHG compared to dispersed/disordered collagen molecules. This is especially important for the forward (F) and backward (B) directions. The ratio of F_{SHG}/B_{SHG} depends on the fibril size. For thicker fibrils forward SHG is predominant while for thinner it tends to become equal, although forward signal is always stronger. This means that the F_{SHG}/B_{SHG} ratio can be used to evaluate fibril's size, even in the range of 10–30 nm that cannot be optically resolved [7]. SHG also depends on the light polarization with respect to the fibril's direction, becoming stronger when both are aligned. This can be used to reveal the orientation angle of individual macromolecular SHG scatterers [8]. In highly scattering or thick specimens, however, both, light directionality and polarization selection rules, are relaxed due to "multiple reflections" inside the sample.

The non-centrosymmetric structure of fibrillar collagen makes it the major source of the SHG signals in biological materials [1, 4, 9, 10]. Collagen forms the structural network of the extracellular matrix (ECM) in tissue and plays an important role during epithelial tumor progression. Thus, changes in collagen content and organization are biomarkers of tissue invasion and can provide insights into the factors that facilitate this process.

SHG has already been shown to have potential applicability for cancer diagnosis by revealing changes in the ECM in tumors relative to normal tissues [11]. Because fibrillar type I collagen is by far the major structural component of the ovarian stroma, SHG is well-suited for probing morphological and structural changes associated with epithelial ovarian cancer, which is responsible for the highest mortality among gynecologic cancers. It is imperative, therefore, to develop early diagnosis methods, before the growth of the tumor, to improve its treatment. Indeed, in the last five years a few groups used combined SHG and fluorescence imaging to show striking morphological changes in malignant ovarian tissues [12–14]. Recently, we used stored H&E stained samples to demonstrate, that SHG and other nonlinear microscopy techniques can differentiate between cancerous and healthy ovarian tissue [15]. We showed that SHG-specific features such fibers orientation and organization of the collagen structure were potentially associated with morphological alterations in the benign, borderline, and malignant samples of serous type ovarian tumors. An advantage of SHG compared with other visualization techniques, such as bright field H & E images, is the SHG selectivity, which is blind to the background populated with too many other things and only sees the collagen fibril's pattern. This allows an automatic digital imaging processing of collagen network only. This kind of discrimination is hard to be performed with non selective imaging techniques.

The purpose of the present work was to extend our previous analysis performed in serous ovarian tumor [15] to the following varieties of human ovarian epithelial tumors: serous, mucinous, endometrioid and mixed types. We evaluate the three subtypes of serous and mucinous tumors classified as adenomas, borderline tumors and adenocarcinomas. TPEF was used mainly to identify epithelium/stromal interface and SHG to determine collagen fiber orientations in the ovarian stroma. Three scoring methods were tested: the first method was based on the calculation of the collagen fiber angle relative to the tumor epithelium to quantify and measure previously defined tumor-associated collagen signatures (TACS) [16]. Keely and coworkers characterized three TACS, which are reproducible during defined stages of tumor progression [17]. These signatures are characterized by the presence of dense collagen localized around small tumors during early disease, called TACS-1; collagen fibers that are parallel to the tumor boundary (around 0 deg.), called TACS-2; and collagen fibers that are perpendicular to the tumor boundary (around 90 deg.) in the invasive phase of disease, called TACS-3. The second used the Fourier domain to analyze the aspect ratio (AR) of the bidimensional intensity distribution of the fast Fourier transform (FFT) images. This method allowed the characterization of the SHG images based on their anisotropy. The third, used only for serous and mucinous tumors, was the gray-level co-occurrence matrix (GLCM) analysis of the images. GLCM is a good method to analyze texture patterns, providing information on the spatial relationships between pixel brightness values in an image. It creates a matrix based on the amount of difference between the neighbor's pixels. Different methods of analysis and quantifications can be performed used with the GLCM matrix, but for this work we only used the correlation. This measurement allowed us to characterize tissues by estimating the typical dimensions within which collagen maintains its organization.

Large differences were observed in the structure and distribution of collagen fibers in the stromal component of the tumor between malignant neoplasm and normal samples. We demonstrated that TACS-3 is observed in the four types of malignant human ovary tumor, for the first time. Our results indicated that the combination of different image-analysis approaches presented here may represent a powerful tool to investigate collagen organization and remodeling of extracellular matrix in ovarian carcinogenesis processes.

## 2. Material and methods

2.1 Ovarian samples

Tissues were obtained from the archives of Department of Pathology of the University Hospital of Campinas, SP, Brazil. The research protocol was approved by the Ethics Committee of the Faculty of Medical Sciences, Unicamp – N° 1437/2001. Because this is a retrospective study with paraffin tissue blocks, the ethics committee exempted informed consent. All procedures were in accordance with the Declaration of Helsinki and the ethical principles of the medical community. Tissues of 4 μm sections were examined either unstained or after H & E-staining using standard techniques. Some adjacent sections were stained with Picrosirius red (Polyscience, Inc., Warrington, Pennsylvania) for optical collagen detection. The sections were rinsed in water and incubated with 0.5% aqueous solution of Picrosirius

red for 1 h at room temperature before rinsing with 0.5% acetic acid (Merck®, Darmstadt, Germany).

Each H & E-stained tissue section was diagnosed by experienced pathologist, based on established World Health Organization histological classification for ovarian neoplasm [18]. The histological diagnosis was determined according to the evaluation of multiple sections from each specimen. In total, 42 ovarian specimens were acquired from different patients (median age, 43 years; range, 21–72) and classified as normal ovarian tissue (5 cases), serous tumors (18 cases) mucinous tumors (11 cases), endometrioid tumors (4 cases) and mixed tumors (4 cases). Serous tumors included: adenoma ($n = 4$), borderline ($n = 3$), and adenocarcinoma ($n = 11$); while the mucinous tumors were: adenoma ($n = 4$), borderline ($n = 2$), and adenocarcinoma ($n = 5$).

2.2 Optical setup

Figure 1a shows the experimental setup. The system consisted of an inverted microscope Axio Observer Z.1 equipped with a Zeiss LSM 780-NLO confocal scan head (Carl Zeiss AG, Germany). The excitation beam was provided by a mode-locked Ti:Sapphire laser (Spectra-Physics. Irvine, USA) emitting 100-fs width pulses at a 80 MHz repetition rate, at the wavelength of 940 nm and an average power at the sample of 10 mW. This laser system was equipped with a DeepSee for group velocity dispersion compensation and an acousto-optic modulator (AOM) for laser power attenuation. The beam was coupled
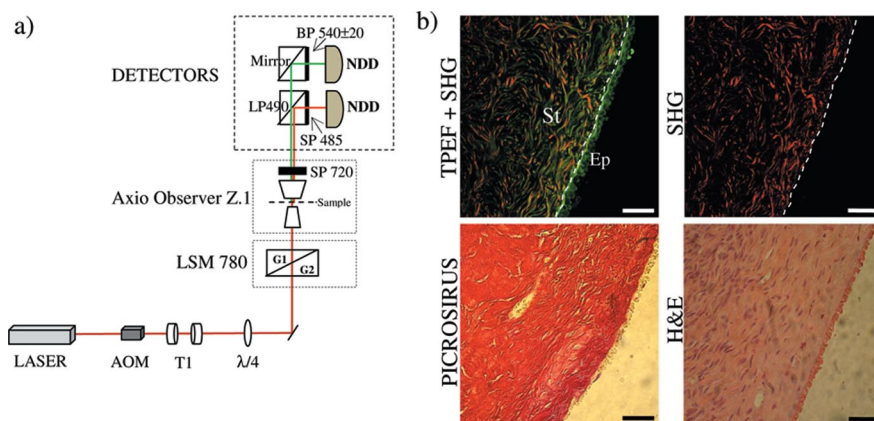
Figure 1 (online color at: www.biophotonics-journal.org) (**a**) Experimental setup to TPEF and SHG microscopy based on an inverted microscope Axio Observer Z.1 and LSM 780-NLO confocal scan head (Carl Zeiss AG, Germany), AOM: acoust-optic modulator, T₁: telescope, λ/4: quarter waveplate, G1/G2: galvanometer mirrors, SP: short-pass filter, BP: band-pass filter, LP: long-pass filter, NDD: Non Descanned Detector. The SHG (red lines) and TPEF (green lines) are collected in a transmitted light configuration. (**b**) Representative TPEF and SHG images obtained with the setup show in a) and the images below shows serial section of picrosirius stained for corroboration of collagen and classical H&E stained sample used for diagnosis. S: stroma, Ep: epithelium, stroma/epithelium interface is indicated with white outline. Scale bars = 20 μm.

to the scan head after a collimating telescope (T1). We used circular polarized light to avoid anisotropies for different fibril's directions. To do that we placed a broadband quarter waveplate (λ/4-Newport) in the laser beam before the microscope scan head and rotated this plate until the light power after the objective did not change with a rotation of a polarizer.

The beam was focused onto the sample by a 40×/1.30 NA oil immersion objective (EC Plan-Neofluar Carl Zeiss AG, Germany). The forward propagating SHG (470 nm) and two-photon fluorescence signals (>490 nm) were collected by the condenser lens 0.55 NA – WD 26 mm (Carl Zeiss) and acquired simultaneously by non-descanned detector (NDD) after a blocking filter SP720 (Omega Filters) to prevent back-reflected laser light. A filter cube with a dichroic LP490 nm wavelength (Carl Zeiss part number 1481-247) and a filter SP485 nm wavelength (Carl Zeiss part number 1481-370) were placed in front of the SHG detector to cut out unwanted fluorescence light from the SHG channel. Other filter cube with a mirror (Carl Zeiss part number 1512-461) and a narrow (20 nm FWHM) BP540 filter (Carl Zeiss part number 1443-332) was used to detect TPEF signal.

Figure 1b shows representative images acquired with this configuration, displaying representative TPEF and SHG images (with 512 × 512 pixel spatial resolution) and serial section stained with picrosirius red and standard H & E for collagen detection and morphological identification respectively. The stained images were acquired with a charge-coupled device (CCD) color camera (DFK 31AF03, The Imaging Source, Germany) placed in the front port of the microscope. TPEF is generated fundamentally by the eosin fluorescence and, for all cases, we used this signal to identify epithelial/stroma interface only (dashed white line). A SHG signal without fluorescence contamination was confirmed by the wavelength range, half of the excitation, of the signal, observed with the Avalanche Photodiodes (APD) array of the LSM-780 Zeiss scan head CCD. Further confirmation was performed detecting this signal with the FLIM system (data not shown) that only presented the instantaneous, within the instrument response function, signal expected for the SHG without any lifetime. The present confirmation was very similar to one we performed this year in a similar setup [19].

2.3 Collagen quantification

All calculations were performed by using ImageJ (v1.45) software (NIH). The methods presented
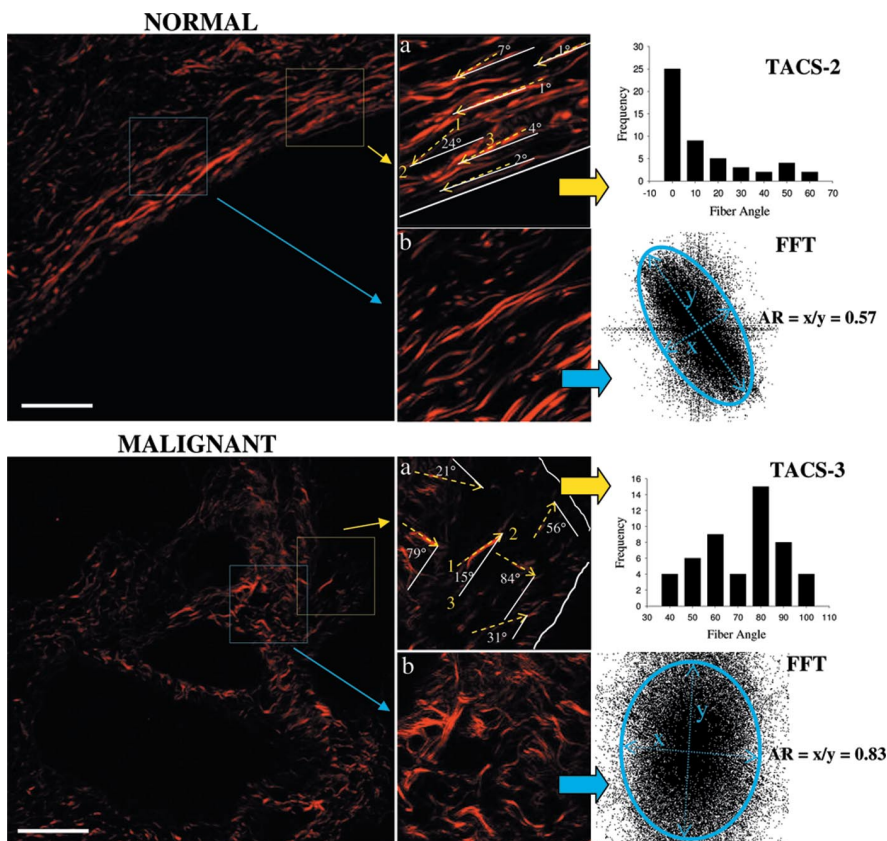
Figure 2 (online color at: www.biophotonics-journal.org) Diagram of the measurements from SHG images in normal and malignant tissues. Inset *a*, tumor-associated collagen signatures (TACS), was done measuring the collagen fiber (yellow arrows) angle (white numbers) relative to the epithelium alignment (white line). Angle tool measured an angle defined by three points (yellow numbers). Only six fibers are represented for demonstration. Total distributions of fibers are presented in a histogram. Inset *b*, representative region used to calculate the FFT transforms and correspondent fit to ellipse (blue) to estimate the anisotropy. *x*: minor axis, *y*: major axis, AR: aspect ratio. Scale bars = 20 µm.

were selected because they have already been successfully used in other analysis of diseases related to collagen [11, 15, 20]. All evaluations were performed in specific regions of interest (ROI) selected over cross-sectional imaging. The numbers and size of ROIs analyzed in each measurement are shown in the respective figures. Because all data came from a digital analysis of the images and all the processing was done automatically, a blind analysis was not necessary.

2.3.1 TACS analysis

The collagen fiber angle relative to the tumor boundary was quantified. We select collagen fibers (yellow arrows, Figure 2 inset a) that were clearly visible and located no more than 30 μm of the epithelium. Given that tumor boundary is not readily identifiable, expert pathologist based in H & E images selected the epithelial zone that present abnormal appearance and this region was considered as the tumor boundary (white line, Figure 2 inset a).

Fiber angle was measured using angle tool from ImageJ toolbar, which measured the angle defined by three points (Figure 2 inset a). The point selection used the following criteria: the first point was a point along the fibril; the second one was the fibril extreme closest to the epithelium (edge) of the tumor; and the third one any point that connected to the first draws a line parallel to the epithelium. Three different images for each type of samples (normal, serous adenocarcinoma, mucinous adenocarcinoma, endometrioid and mixed tumors) were analyzed, selecting an average of 50 fibers for each. In total, 150 angles were measured for each type of tumor. From previous established definition of collagen organization [16], collagen fibers oriented parallel or perpendicular to the epithelium (tumor boundary) were classified as TACS-2 and TACS-3 respectively.

2.3.2 Aspect ratio analysis

To perform the AR analysis we used Fast Fourier Transform (FFT), which is a good method to assign a degree of organization to images. The FFT image of a set of aligned fibers will have higher values along the direction orthogonal to the direction of the fibers and its intensity plot looks like an ellipse. If the fibers are perfectly aligned the ellipse will collapse to a line. For randomly oriented fibers, however, the intensity plot of the corresponding FFT image looks like a circle. Therefore, the anisotropy of the image was evaluated performing an elliptic fit on the thresholded FFT images and by calculating the

ratio between its short and long axes, i.e., its aspect ratio (Figure 2, inset b) [21]. The sample is more anisotropic as the AR is close to 0, whereas it is more isotropic when the AR is close to 1.

To perform the calculations four ROI (120×120 pixel side squared) in the SHG images were selected. This was done to make sure that mainly collagen network in the vicinity of the epithelium was used for the FFT analysis, because this is the region responsible for the invasion of the stroma. The square ROI is required by the FFT procedure of ImageJ, based on an implementation of the 2D Fast Hartley Transform [22]. FFT can be implemented with the commands FFT of the menu Process of ImageJ.

2.3.3 Correlation analysis

We characterized tissues with GLCM methods by estimating the typical dimensions within which collagen maintains its organization. We used the correlation of the image with itself with a pixel separation translated from one to 12 or 18 pixels. The feature was averaged at angles $\theta = 0$, 90, 180, and 270 degrees to take into account the fact that these images do not have a specific spatial orientation. We measured the distance where correlation falls to 1/2, expressed in microns. To perform the calculations three ROI (101×101 pixel side squared) in the SHG images near the epithelium were selected. Correlation was measured using GLCM-Texture plugin from ImageJ, which was described by Walker and collaborators [23].

2.4 Statistical analysis

For multi-group comparisons, one-way analysis of variance (ANOVA) with a *post-hoc* Tukey-Kramer test was used. We performed *t*-testing for two-group comparisons. The level of significance employed was significant (*) $p < 0.05$ and very significant (**) $p < 0.01$. Data were analyzed with SPSS 10.0 software.

3. Results

First, to confirm that SHG visualize fundamentally collagen type I the tissue sections were stained with Picrosirius red, which also binds to other collagen types, such as collagen II, III, IV, and V [24–26]. Picrosirius red is an acidic dye which strongly reacts with collagen basic amino acids and also enhances
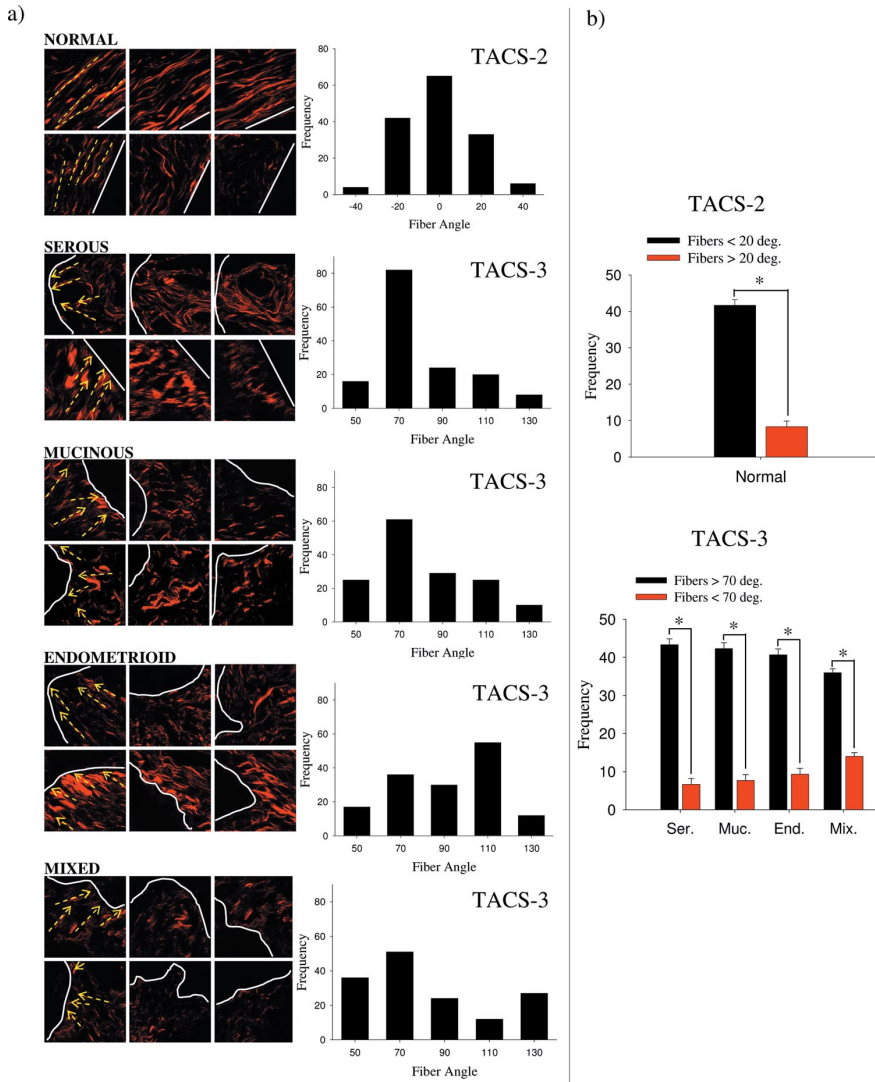
Figure 3 (**a**) (online color at: www.biophotonics-journal.org) Analysis of collagen fiber (yellow arrow) angles relative to the epithelial boundary (white line) for normal ovary, serous adenocarcinoma, mucinous adenocarcinoma, endometrioid, and mixed tumors of the ovary. Three regions (200 × 200 pixels) enlarged from two representative biopsies for each tumor and normal tissues analyzed are presented. TACS histograms from normal samples displayed principally TACS-2. In contrast the serous, mucinous, endometrioid, and mixed samples displayed mainly TACS-3. Values on the histogram were calculated from three biopsies for each type of tissue. An average of 50 fibers in each biopsy was quantified giving a total of 150 fibers for type of tissue. (**b**) Quantitative analysis of fibers of collagen that are principally distributed around 0 deg (angle <20 deg) in normal samples, and around 90 deg (angle >70 deg) in tumors samples. Ser: serous, Muc: mucinous, End: endometrioid, Mix: mixed. Asterisks (*) indicate $p < 0.05$ difference from normal samples.

the birefringence of collagen fibers. Figure 1b compares the collagen network visualized by SHG (dark red), collagen-Picrosirius (light red) and H & E-stain sections (pink) in normal ovarian tissue. All three types of images displayed collagen type I fibers. Same results were found with stained malignant ovarian tissues (data not shown).

Next, we quantified the collagen fiber angle in relation to the epithelium alignment. Three biopsies for each type of tissue (normal, serous adenocarcinomas, mucinous adenocarcinomas, endometriod, and mixed tumors) were analyzed. An average of 50 fibers in each biopsy was quantified giving a total of 150 fibers for type of tissue. Figure 3a shows three regions (200 × 200 pixels) enlarged from two representative biopsies for each tumor and normal tissues analyzed. Only for reference, we indicated in one region, collagen fibers selected to measure the angle (yellow arrows). The histograms depict the total distribution of the fibers analyzed. In normal tissues we found a distribution of collagen fiber angles around 0 deg (83% the fibers). This corresponds to TACS-2, which is associated with noninvasive regions. On the opposite way, in all malignant ovarian tumors analyzed we found distributions of collagen fiber angles around 90 degrees in relation to the epithelium boundary that correspond to TACS-3. Serous and mucinous adenocarcinomas showed higher number of fibers around 90 deg (79% and 75% respectively), while endometrioid and mixed types showed less number of fibers with this inclination (65% and 56% respectively). Analyzing 50 fibers in three images for each type of ovarian samples we quantified the number of fibers of collagen that are principally distributed around 0 deg (angle <20 deg) in normal samples, and around 90 deg (angle >70 deg) in tumors samples (Figure 3b). In normal samples, the number of fibers with angle <20 deg was greater than fibers with angle >20 deg. These values were found to be statistically different at the 0.05 level after a two-

sample statistical t-test. In all tumor samples analyzed the number of fibers with angle >70 deg was greater than fibers with angle <70 deg. These values were found to be statistically different at the 0.05 level after a two-sample statistical t-test; confirming the TACS-3 classification for tumor tissues.

Resuming, our results confirm the existence of a correlation between TACS-3 and malignancy. TACS-3 was not observed around the entire perimeter of each tumor region, but rather locally. Therefore, the frequency of TACS-3 could be indicative of the primary sites of invasion.

In the second part of the study we estimated the different orientations of collagen fibers in the ovarian stroma by anisotropy calculations. To perform the calculations four ROI (120×120 pixel side squared) in each sample were selected (normal: $20\,ROI = [n = 5] \times 4$, serous: $44\,ROI = [n = 11] \times 4$, mucinous: $20\,ROI = [n = 5] \times 4$, endometrioid: $16\,ROI = [n = 4] \times 4$, and mixed: $16\,ROI = [n = 4] \times 4$). With this selection we can cover the entire stroma near the epithelium. Figure 4a shows repre-

sentative H & E-stained and the correspondent TPEF + SHG images of all different histological types of ovarian samples analyzed. For clarity only one ROI shows (in the inset) the SHG signal and the correspondent FFT image. The results obtained show that FFT images of normal ovary have a more elliptical profile (image containing a set of aligned fibers) when compared to the FFT images of malignant ovary, which presents a more circular configuration (image with randomly oriented fibers). Figure 4b shows the averaged AR on all ROI of the examined samples. In ovarian carcinomas, AR values were 0.78 ± 0.03, 0.75 ± 0.04, 0.72 ± 0.02 and 0.76 ± 0.02 for serous ($n = 44$), mucinous ($n = 20$), endometrioid ($n = 16$) and mixed ($n = 16$) histological types respectively. These values were statistically significant ($p < 0.05$) after a two-sample statistical t-test, when compared to normal ovary, whose AR value was 0.57 ± 0.01 ($n = 20$). This result confirms the fact that normal ovary are more organized tissues as compared to malignant ovarian tumors.

Figure 4 (online color at: www.biophotonics-journal.org) (**a**) Representative bright field H & E-image and TPEF + SHG images (512512 pixels) at a two-photon excitation wavelength of 940 nm of tissues diagnosed as normal ovary, serous, mucinous, endometrioid and mixed adenocarcinomas. Boundary epithelium (white outline) and four different ROI (120×120 pixels, yellow squared) where the FFT was performed are shown. FFT intensity images obtained after 2D-DFT of the only one ROI are shown below SHG images. (**b**) Results of the AR of ovarian samples averaged on all ROI examined. For calculations four ROI in each sample were selected (normal: $20\,ROI = [n = 5] \times 4$, serous: $44\,ROI = [n = 11] \times 4$, mucinous: $20\,ROI = [n = 5] \times 4$, endometrioid: $16\,ROI = [n = 4] \times 4$, and mixed: $16\,ROI = [n = 4] \times 4$). Each bar represents the mean $\pm$S.D. of independent 2D-DFT. Nor: normal, Ser: serous, Muc: mucinous, End: endometrioid, Mix: mixed. Asterisks (**) indicate $p < 0.01$ difference from normal samples. All scale bars are 20 µm.
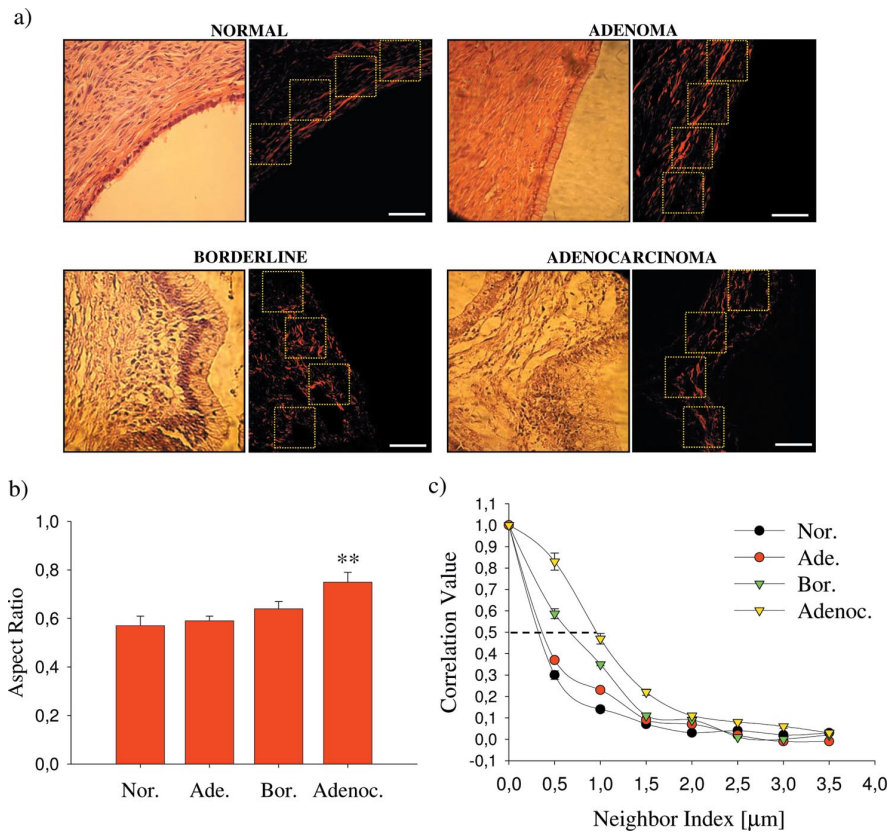
a)

b)

c)
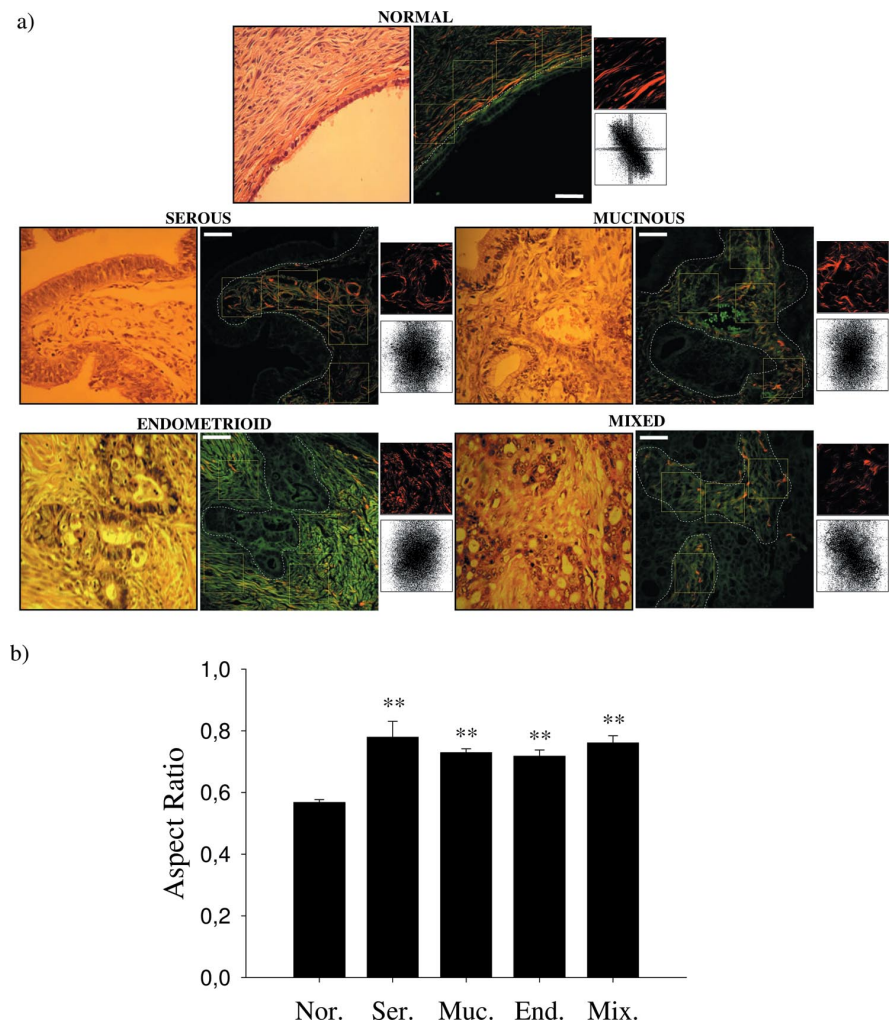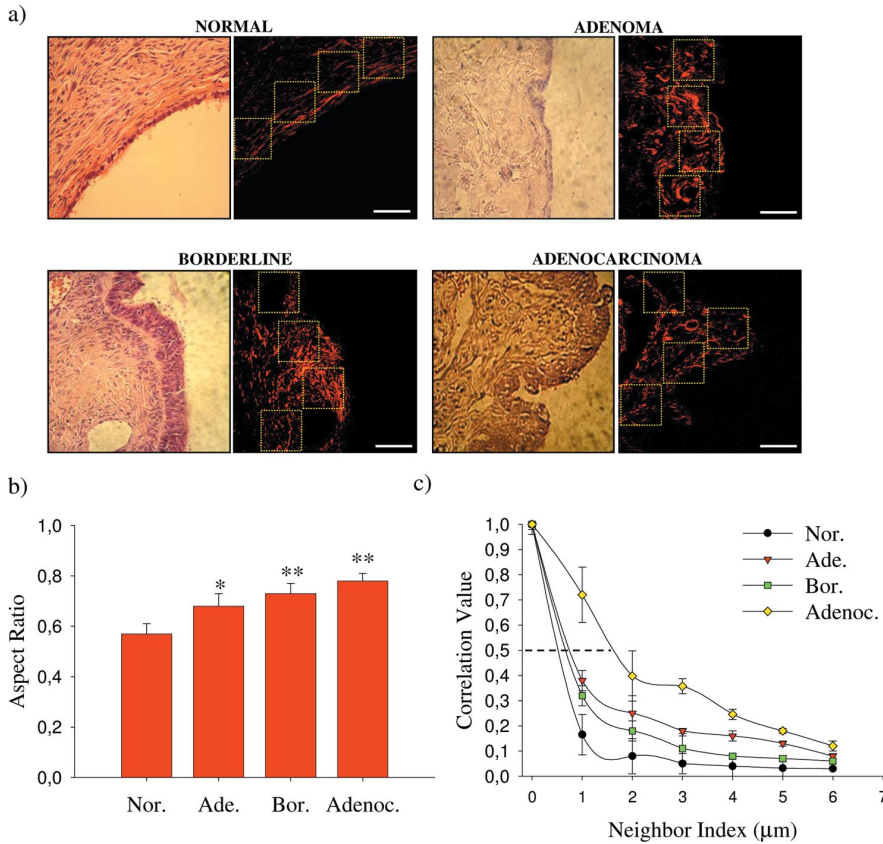
Figure 5 (online color at: www.biophotonics-journal.org) (**a**) Representative bright field H & E-image and SHG images (512512 pixels) at a two-photon excitation wavelength of 940 nm of tissues diagnosed as normal ovary, serous adenoma, serous borderline tumor, and serous adenocarcinoma. The four different ROI (yellow squared) where the FFT was performed are shown. All scale bars are 20 μm. (**b**) Results of the aspect ratio of ovarian samples averaged on all the examined ROI. Four ROI (120×120 pixel side squared) in each subtype serous sample were selected (normal: 20 ROI = $[n = 5] \times 4$, adenoma: 16 ROI = $[n = 4] \times 4$, borderline: 12 ROI = $[n = 3] \times 4$, and adenocarcinoma: 44 ROI = $[n = 11] \times 4$). Each bar represents the mean $\pm$S.D. of independent 2D-DFT. Asterisks (*; **) indicate a $p < 0.05$ and $p < 0.01$, respectively, differences from normal samples. (**c**) Correlation values in serous ovarian tumors versus distances pixels; the correlation for distances ranging from 1 to 18 pixels (0.35–6.0 μm) in three ROI of 101×101 pixel of interest for each biopsy was calculated. Dotted line = $Corr_{50}$ value. Nor: normal, Ade: adenoma, Bor: borderline, Adenoc: adenocarcinoma.

Finally, we performed a complete analysis in serous (Figure 5) and mucinous (Figure 6) subtypes, since they are the more frequent alterations present in epithelial ovarian cancer. Specifically, adenomas, borderline and adenocarcinomas of serous and mucinous subtypes were compared with normal tissues. Figure 5a shows the classical histological H & E-stained section and the correspondent SHG images of the several ovarian tissues with serous differentiation and ROI selected for quantification. Figure 5b shows the AR average value on all ROI examined. Four ROI (120×120 pixel side squared) in each subtype serous sample were selected (normal: 20 ROI = $[n = 5] \times 4$, adenoma: 16 ROI = $[n = 4] \times 4$, borderline: 12 ROI = $[n = 3] \times 4$, and adenocarcinoma: 44 ROI = $[n = 11] \times 4$). AR increases progressively (0.68 ± 0.05, 0.73 ± 0.04 and 0.78 ± 0.03) and signifi-

cantly after a two-sample statistical t-test, when compared to normal specimens (0.57 ± 0.04). Figure 5c shows results of texture analysis, where normal fibrils correlation falls off sharply with distance, revealing isolated thin fibrils. On the other hand, correlation for the fibrils in adenocarcinomas remained elevated for larger distances, implying fibrillar structures poorly defined. Consistent with qualitative appearances, we found evaluating three ROI (101×101 pixel side squared) in the SHG images near the epithelium, that the correlation remained higher in malignant tissues with the $Corr_{50}$, the pixel distance where the correlation dropped below 50% of the initial value, significantly greater in adenocarcinomas compared with normal ovarian (Figure 5c; $P < 0.05$, ANOVA).

Figure 6a shows different mucinous ovarian subtypes and Figure 6b shows the AR average value on

a)

b)

c)

Figure 6 (online color at: www.biophotonics-journal.org) (**a**) Representative H & E-staining and SHG images (512512 pixels) at a two-photon excitation wavelength of 940 nm of tissues diagnosed as normal ovary, mucinous adenoma, mucinous borderline tumor, and mucinous adenocarcinoma. The four different ROI (yellow squared) where the FFT was performed are shown. All scale bars are 20 μm. (**b**) Results of the aspect ratio of ovarian samples averaged on all the examined ROI. Four ROI (120×120 pixel side squared) in each subtype mucinous sample were selected (normal: 20 ROI = [$n = 5$] $\times$ 4, adenoma: 16 ROI = [$n = 4$] $\times$ 4, borderline: 8 ROI = [$n = 2$] $\times$ 4, and adenocarcinoma: 20 ROI = [$n = 5$] $\times$ 4). Each bar represents the mean ±S.D. of independent 2D-DFT. Asterisks (**) indicates a significant ($p < 0.01$) difference from normal samples. (**c**) Correlation values in serous ovarian tumors versus distances pixels; the correlation for distances ranging from 1 to 12 pixels (0.35–3.0 μm) in three ROI of 101×101 pixel of interest for each biopsy was calculated. Dotted line = $Corr_{50}$ value. Nor: normal, Ade: adenoma, Bor: borderline, Adenoc: adenocarcinoma.

all ROI examined. Four ROI (120×120 pixel side squared) in each subtype mucinous sample were selected (normal: 20 ROI = [$n = 5$] $\times$ 4, adenoma: 16 ROI = [$n = 4$] $\times$ 4, borderline: 8 ROI = [$n = 2$] $\times$ 4, and adenocarcinoma: 20 ROI = [$n = 5$] $\times$ 4). For these tumors only adenocarcinomas presents sta-

tistically highly significant differences (0.75 ± 0.04). However, the correlation values are similar to those found in serous tumors, which means that the $Corr_{50}$ was significantly greater in adenocarcinomas compared with normal ovarian (Figure 6c). Table 1 summarizes and compares the previous results found for

Table 1 Aspect ratio (AR) values.

Ovarian tissues				
Normal	Tumor types	Adenoma	Borderline	Adenocarcinoma
0.57 ± 0.04	Serous	0.68 ± 0.05[*, §, φ]	0.73 ± 0.04[**, §, φ]	0.78 ± 0.03[**]
	Mucinous	0.59 ± 0.02	0.64 ± 0.03	0.75 ± 0.04[+]

*, **: $p < 0.05$ and $p < 0.001$, respectively, according to *t*-test for normal, benign, borderline and malignant subtypes.
§: $p < 0.05$, according to ANOVA test applied within the serous specimens.
+: $p < 0.05$, according ANOVA test applied within the mucinous specimens.
φ: $p < 0.05$, according ANOVA test applied between serous and mucinous specimens.

serous and mucinous ovarian tumors. These data confirm that the normal ovary presents a more organized epithelium when compared to adenocarcinomas. By denoting SA, SB and SAC for serous adenoma, borderline and adenocarcinoma tumors respectively and MA, MB and MAC for the three mucinous subtypes and use the notation $A = B$ to mean that A and B are not statistically different and $A \neq S$ to mean that A and B are statistically different we can say that $SA \neq SB \neq SAC$, $MA = MB \neq MAC$, $SA \neq MA$, $SB \neq MB$ but $SAC = MAC$. In summary, the results together strongly indicate that collagen presentation in normal and tumoral tissues obeys specific patterns which can be detected with SHG signals.

4. Discussion

In this study, we acquired SHG-microscopy images of collagen fibers from human ovarian stroma to determine the remodeling of the extracellular matrix during the malignant process of carcinogenesis in ovary. Using three scoring methods (signature of collagen, anisotropy and correlation index), we observed significant differences between the arrangement and structure of collagen matrix of benign and malignant ovarian specimens. For the first time four different types of ovarian tumors and their different categories were analyzed using SHG microscopy.

In the last years, SHG has emerged as a powerful nonlinear optical contrast mechanism for biological and biophysical imaging applications. In general the recent reports have focused on visualizing collagen fibers in a variety of connective tissues from skin, bone, cartilage, tendon, hematopoietic tissue, and cornea as well as fibrotic lesions in internal organs [27–31]. A considerable optimism exist on that SHG imaging may be translated to clinical applications supplementing the well established histological methods for tumor detection. Given our previous experience and the results of this work, we believe that SHG signals from collagen fibers could be also a promising imaging modality to understand carcinogenesis [15, 32]. Besides, this technique has several advantages. First, collagen features are stable and robust, persisting even when tissues have not been fixed in a timely manner, and these features are maintained under various tissue-processing approaches [16, 33]. Second, SHG imaging can be performed in unstained or H & E-stained slides, and thus requires no additional staining procedures for collagen identification such as picrosirius red. Furthermore, SHG microscopy can be used to reveal details of macromolecular and supramolecular assemblies which are not possible through other techniques such as fluorescence imaging.

Our results from TACS and anisotropy measurements indicate that collagen networks in serous, mucinous, endometrioid and mixed tumors were strikingly different from the corresponding normal tissue, which shows that structural modifications of the fibrillar collagen matrix in malignant tissues exist and that these modifications can be measured with specific optical techniques. We observed structures compatible with remodeling of extracellular matrix, being the first study to identify TACS-3 signatures in all human ovarian tumors analyzed. These results also agree well with other groups' reports which suggested that regions containing TACS-3 correspond to sites of focal invasion into the stroma [16, 17]. For example, others have observed that tumor cells preferentially invade along straightened, aligned collagen fibers, which can promote intravasation [16, 34–36]. Moreover, we observed a gradual transformation of TACS-2 into TACS-3 in serous ovarian tumors as the ovarian stromal configuration passes from normal to an abnormal appearance. Adenomas show mostly TACS-2, borderlines present both TACS-2 and TACS-3 and serous adenocarcinomas mostly TACS-3 distribution [15]. Similarly, the collagen alignment was used to quantify local invasion with the level of TACS-2 and TACS-3 in breast tumors and shows that the increased invasiveness is not only the result of earlier tumorigenesis that had more time to progress, but it is also due to tumor cells that are fundamentally more invasive because they arose within collagen-dense tissues [17]. Recently, Conklin and coworkers reported that TACS-3 signature is robust and significantly associated with disease outcome of human breast carcinoma and could be used as an adjunct to the histopathologic process to help inform patient diagnosis [37]. In line with this suggestion we believe that TACS-3 could be a novel biomarker to be associated with the ovarian malignant disease.

Several studies have shown that the collagen fibers are irregularly disordered without well-defined orientation in pathological samples, while the morphology of the collagen fibers is highly arranged in normal samples [12, 38–42]. This means that a detailed knowledge of the collagen morphology is very important because structural modifications of the fibrillar matrix are associated with various physiologic processes including cancer [9]. It is known that biopsies from patients with epithelial ovarian cancer exhibited a loss of fine structure and structural organization with wavy, collagen bundles, whereas the normal tissue exhibited normotypic structured collagen fibrils near the epithelial surface [11]. In this work, using anisotropy and correlation scoring methods, we confirmed that all histological types of tumors show a more disorganized stroma with respect to the normal tissues. One important finding was that it is possible to discriminate between serous

FULL ARTICLE

Table 2 Summary of the different techniques for the analysis of collagen fibers in ovary stroma.

Technique	Measured Variable	Values	Conclusion	Calculation
TACS	Fiber angle (relative to epithelium)	TACS-2 ($\theta \cong 0$ deg) TACS-3 ($\theta \cong 90$ deg)	Normal ovaries present TACS-2 while adenocarcinomas show TACS-3, which may be indicative of the invasive and metastatic growth potential.	Angle tool of ImageJ
AR	Fiber direction	AR = 0 (anisotropic) AR = 1 (isotropic)	Normal ovaries fibers show isotropic behavior. While in adenocarcinomas the fibers are more anisotropic.	FFT process of ImageJ
Correlation	Fiber separation	$C \cong 1$ (displaced image = non displaced one, non-periodic fibers) $C \cong 0$ (displaced image $\neq$ non displaced one, periodic fibers)	Normal ovaries show more defined and periodic fibers. While adenocarcinomas tissues show more random and non-periodic fibers.	GLCM plugin of ImageJ

TACS: Tumor-Associated Collagen Signatures, AR: Aspect Ratio, θ: angle, C: correlation, FFT: Fast Fourier transform, GLCM: Gray-Level Co-occurrence Matrix.

adenoma from mucinous adenoma and serous borderline from mucinous borderline tumors. Unlike ovarian serous tumors, which are relatively homogeneous in their cellular composition and degree of differentiation, mucinous tumors are frequently heterogeneous, with mixtures of benign, borderline, and malignant elements often found within the same neoplasm, in a spectrum pattern. They are commonly large tumors that occasionally reach massive proportions. The heterogeneity in these mucinous tumors suggests that malignant transformation is sequential and slow, progressing from adenoma to borderline tumor and, finally, to invasive carcinoma [43]. This behavior is probably reflected in a more organized stroma.

In conclusion, we have tested the capability of SHG microscopy and different image-pattern analysis approaches to characterize different ovarian tumors with some particular stromal disorder. We found that SHG imaging allows the visualization of collagen alteration with epithelial tumor progression and to quantify features of collagen-fibril bundles orientation and collagen fibril structure that can establish a quantitative link between collagen alteration and epithelial tumor progression. The methods presented in this work represent a promising analysis/ scoring tool for cancer pathogenesis and diagnosis (Table 2). We believe that a combination of these methods can give complementary information to facilitate the identification of alterations in ovarian stroma. The capability of quantifying collagen altera-

tion with epithelial tumor progression renders SHG microscopy an *in situ* histological tool that is free from the labeling requirement of conventional methods. The present study will provide the groundwork for the exploitation of SHG based analysis in clinical settings.

Javier Adur received his MSc degree in Biomedical Engineering in 2006 at the University National of Entre Ríos, Argentina, and his Ph.D. in Biology in 2008 at the University National of Litoral, Argentina. Since 2004, he has been Assistant Professor at the School of Engineering at the National University of Entre Ríos. He is currently a visiting professor at "Gleb Wataghin" Institute of Physics, State University of Campinas (UNICAMP), Brazil. His research involves nonlinear microscopy techniques of diseased tissues.

Vitor Bianchin Pelegati received his degree in Physics in 2006, and the MSc in Physics in 2010, from the State University of Campinas (UNICAMP), Brazil. He is cur-

rently conducting his Ph.D. in Physics, on the subject of nonlinear optical microscopy techniques, such as CARS, SHG, THG and SFG.

Andre A. de Thomaz received his degree in Physics in 2004, and the MSc in Physics in 2007, from the State University of Campinas (UNICAMP), Brazil. He is currently conducting his Ph.D. in Physics, on the subject of fluorescence dynamics of quantum dots. His research interests are: single photon/multiphoton microscopies (fluorescence, SHG, THG, FLIM, CARS), optical tweezers and quantum dots for biological applications.

Mariana Ozello Baratti is senior technician at the National Institute of Photonics Applied to Cell Biology-INFABiC. She graduated in Biology in 2004 at University PUC-Campinas, and received her Ph.D. in Molecular Biology in 2011 at the Laboratory of Molecular and Cellular Biology at the Hematology and Hemotherapy Center at the University of Campinas (UNICAMP), Brazil. At INFABiC, she currently assists researchers in the applications of techniques using microscopy single/multiphoton (Confocal, FRET, FRAP, time lapse) and nonlinear optical techniques (FLIM, SHG, THG and CARS).

Liliana Andrade received her MD and Ph.D. from the University of Campinas. She is a pathologist responsible for gynecologic pathology and professor of the Department of Pathology, Faculty of Medical Sciences of University of Campinas, UNICAMP, Brazil.

Hernandes Faustino Carvalho received his degree in Biology from State University of Campinas – UNICAMP (1987), his master's (1989) and Ph.D. in Biochemistry (1993). He is currently a full professor at UNICAMP. His research interests are prostate, castration, androgen receptor, development, elastic fibers and extracellular matrix.

Fátima Bottcher-Luiz received her degree in Biology from State University of Campinas – UNICAMP (1979), her master's (1989) and Ph.D. in Human Genetics (1996). Has experience in human reproduction and genetics, focusing on the women health. Her principal topics of research are: tumor cell cultures, breast/ovarian cancer and tumor markers.

Carlos Lenz Cesar received his degree in Physics from Federal University of Ceará (1977), and master's (1979) and Ph.D. (1985) in Physics from State University of Campinas – UNICAMP. He is currently full professor at the Institute of Physics Gleb Wataghin in UNICAMP. His research interests are integrated biophotonics microscopy such as TPEF, CARS, FLIM, FRET, Raman, Hyper-Raman, and micromanipulations using optical tweezers, laser cutting and AFM/tip-enhancement, and quantum dots physics and applications.

References

[1] W. R. Zipfel, R. M. Williams, R. Christie, A. Y. Nikitin, B. T. Hyman, and W. W. Webb, Proc. Natl. Acad. Sci. USA **100**, 7075–7080 (2003).

[2] P. P. Provenzano, K. W. Eliceiri, L. Yan, A. Ada-Nguema, M. W. Conklin, D. R. Inman, and P. J. Keely, Microsc. Microanal. **14**, 532–548 (2008).

[3] W. Denk, J. H. Strickler, and W. W. Webb, Science **248**, 73–76 (1990).

[4] G. Cox, E. Kable, A. Jones, I. Fraser, F. Manconi, and M. D. Gorrell, J. Struct. Biol. **141**, 53–62 (2003).

[5] F. Legare, C. Pfeffer, and B. R. Olsen, Biophys. J. **93**, 1312–1320 (2007).

[6] S. W. Perry, R. M. Burke, and E. B. Brown, Ann. Biomed. Eng. **40**, 277–291 (2012).

[7] R. Lacomb, O. Nadiarnykh, S. S. Townsend, and P. J. Campagnola, Optics. Comm. **281**, 1823–1832 (2008).

[8] S. V. Plotnikov, A. C. Millard, P. J. Campagnola, and W. A. Mohler, Biophys. J. **90**, 693–703 (2006).

[9] A. Zoumi, A. Yeh, and B. J. Tromberg, Proc. Natl. Acad. Sci. USA **99**, 11014–11019 (2002).

[10] R. M. Williams, W. R. Zipfel, and W. W. Webb, Biophys. J. **88**, 1377–1386 (2005).

[11] S. Zhuo, J. Chen, W. G. Wu, S. Xie, L. Zheng, X. Jiang, and X. Zhu, Appl. Phys. Lett. **96**, 1–3 (2010).

[12] N. D. Kirkpatrick, M. A. Brewer, and U. Utzinger, Cancer Epidemiol. Biomark. Prev. **16**, 2048–2057 (2007).

[13] R. M. Williams, A. Flesken-Nikitin, L. H. Ellenson, D. C. Connolly, T. C. Hamilton, A. Y. Nikitin, and W. R. Zipfel, Transl. Oncol. **3**, 181–194 (2010).

[14] O. Nadiarnykh, R. B. LaComb, M. A. Brewer, and P. J. Campagnola, BMC Cancer **10**, 1–14 (2010).

[15] J. Adur, V. B. Pelegati, L. F. Costa, L. Pietro, A. A. de Thomaz, D. B. Almeida, F. Bottcher-Luiz, L. A. Andrade, and C. L. Cesar, J. Biomed. Opt. **16**, 096017 (2011).

[16] P. P. Provenzano, K. W. Eliceiri, J. M. Campbell, D. R. Inman, J. G. White, and P. J. Keely, BMC Med. **4**, 1–16 (2006).

[17] P. P. Provenzano, D. R. Inman, K. W. Eliceiri, J. G. Knittel, L. Yan, C. T. Rueden, J. G. White, and P. J. Keely, BMC Med. **6**, 1–15 (2008).

[18] R. E. Scully, R. H. Young, and P. B. Clement (eds.), Atlas of Tumor Pathology: Tumors of the Ovary, Maldeveloped Gonads, Fallopian Tubes and Broad Ligament, 3rd edn. (Armed Forces Institute of Pathology, Washington, D.C., 1998).

[19] V. B. Pelegati, J. Adur, A. A. De Thomaz, D. B. Almeida, M. O. Baratti, L. A. Andrade, F. Bottcher-Luiz, and C. L. Cesar, Microsc. Res. Tech., DOI: 10.1002/jemt.22078 (2012).

[20] R. Cicchi, D. Kapsokalyvas, V. De Giorgi, V. Maio, A. Van Wiechen, D. Massi, T. Lotti, and F. S. Pavone, J. Biophotonics **3**, 34–43 (2010).

[21] P. Matteini, F. Ratto, F. Rossi, R. Cicchi, C. Stringari, D. Kapsokalyvas, F. S. Pavone, and R. Pini, Opt. Express **17**, 4868–4878 (2009).

[22] A. Arlo Reeves, Thesis for the degree of Master of Science by Thayer school of engineering (Dartmouth College Hanover, New Hampshire, 1990).

[23] R. F. Walker, P. Jackway, and I. D. Longstaff, Int. J. Pattern. Recogn. **17**, 17–39 (2003).

[24] G. Cox, E. Kable, A. Jones, I. K. Fraser, F. Manconi and M. D. Gorrell, J. Struct. Biol. **141**, 53–62 (2003).

[25] L. C. U. Junqueira, G. S. Montes, and E. M. Sanchez, Histochemistry **74**, 153–156 (1982).

[26] M. Strupler, A. M. Pena, M. Hernest, P. L. Tharaux, J. L. Martin, E. Beaurepaire, and M. C. Schanne-Klein, Opt. Express **15**, 4054–4065 (2007).

[27] T. A. Theodossiou, C. Thrasivoulou, C. Ekwobi, and D. L. Becker, Biophys. J. **91**, 4665–4677 (2006).

[28] S. J. Lin, S. H. Jee, C. J. Kuo, R. J. Wu, W. C. Lin, J. S. Chen, Y. H. Liao, C. J. Hsu, T. F. Tsai, Y. F. Chen, and C. Y. Dong, Opt. Lett. **31**, 2756–2758 (2006).

[29] A. M. Pena, A. Fabre, D. Debarre, J. Marchal-Somme, B. Crestani, J. L. Martin, E. Beaurepaire, and M. C. Schanne-Klein, Microsc. Res. Tech. **70**, 162–170 (2007).

[30] C. Odin, Y. Le Grand, A. Renault, L. Gailhouste, and G. Baffet, J. Microsc. **229**, 32–38 (2008).

[31] G. P. Kwon, J. L. Schroeder, M. J. Amar, A. T. Remaley, and R. S. Balaban, Circulation **117**, 2919–2927 (2008).

[32] J. Adur, V. B. Pelegati, A. A de Thomaz, L. D'Souza-Li, M. C. Assunçao, F. Bottcher-Luiz, L. Andrade, and C. L. Cesar, J. Biomed. Opt. **17**, 081407 (2012).

[33] M. W. Conklin, P. P. Provenzano, K. W. Eliceiri, R. Sullivan, and P. J. Keely, Cell. Biochem. Biophys. **53**, 145–157 (2009).

[34] J. B. Wyckoff, Y. Wang, E. Y. Lin, J. F. Li, S. Goswami, E. R. Stanley, J. E. Segall, J. W. Pollard, and J. Condeelis J, Cancer. Res. **67**, 2649–2656 (2007).

[35] W. Wang, J. B. Wyckoff, V. C. Frohlich, Y. Oleynikov, S. Huttelmaier, J. Zavadil, L. Cermak, E. P. Bottinger, R. H. Singer, J. G. White, J. E. Segall, and J. S. Condeelis, Cancer. Res. **62**, 6278–6288 (2002).

[36] P. P. Provenzano, D. R. Inman, K. W. Eliceiri, S. M. Trier, and P. J. Keely, Biophys. J. **95**, 5374–5384 (2008).

[37] M. W. Conklin, J. C. Eickhoff, K. M. Riching, C. A. Pehlke, K. W. Eliceiri, P. P. Provenzano, A. Friedl, and P. J. Keely, A. J. Pathol. **178**, 1221–1232 (2011).

[38] G. Chen, J. Chen, S. Zhuo, S. Xiong, H. Zeng, X. Jiang, R. Chen, and S. Xie, Br. J. Dermatol. **161**, 48–55 (2009).

[39] C. M. Hsueh, W. Lo, S. Lin, T. Wang, F. Hu, H. Tan, and C. Dong, J. Innovative. Opt. Health. Sci. **2**, 45–60 (2009).

[40] K. Lu, S. Zhuo, Z. Hong, G. Chen, X. Jiang, L. Zheng, and J. Chen, J. Innovative. Opt. Health. Sci. **2**, 61–66 (2009).

[41] P. Wilder-Smith, K. Osann, N. Hanna, N. El Abbadi, M. Brenner, D. Messadi, and T. Krasieva, Lasers Surg. Med. **35**, 96–103 (2004).

[42] O. Nadiarnykh, S. Plotnikov, W. A. Mohler, I. Kalajzic, D. Redford-Badwal, and P. J. Campagnola, J. Biomed. Opt. **12**, 051805 (2007).

[43] W. R. Hart, J. Gynecol. Pathol. **24**, 4–25 (2005).